Broadband Noise Characterization of SiGe HBTs Down to 4K

Benserhir, J.; Zou, Y.; Han, H. -C.; Peng, Y.; Charbon, E.

DOI
10.1109/JEDS.2025.3595576

Publication date
2025

Document Version
Final published version

Published in
IEEE Journal of the Electron Devices Society

Received 13 May 2025; revised 17 July 2025; accepted 31 July 2025. Date of publication 4 August 2025; date of current version 27 August 2025.
The review of this article was arranged by Editor P.-W. Li.

Digital Object Identifier 10.1109/JEDS.2025.3595576

Broadband Noise Characterization of SiGe HBTs Down to 4K

JAD BENSERHIR [1] (Member, IEEE), YATING ZOU [2] (Student Member, IEEE), HUNG-CHI HAN [2] (Member, IEEE), YATAO PENG [3] (Member, IEEE), AND EDOARDO CHARBON [2] (Fellow, IEEE)

1 Department of Quantum and Computer Engineering, Delft University of Technology, 2628 CJ Delft, The Netherlands
2 Institute of Electrical and Micro Engineering, AQUA Lab, Ecole Polytechnique Fédérale de Lausanne, 2000 Neuchâtel, Switzerland
3 State Key Laboratory of Analog and Mixed-Signal VLSI, Institute of Microelectronics, and FST ECE, University of Macau, Macau, China

CORRESPONDING AUTHOR: J. BENSERHIR (e-mail: jad.benserhir@epfl.ch)

ABSTRACT This paper provides a comprehensive analysis of the DC and RF behavior of HBTs, spanning temperatures from 350 to 3.8 K. It underscores the necessity of detailed studies for the design of RF circuits for quantum computing, including LNAs, VCOs, and mixers, due to the absence of cryogenic models. The DC gain shows betas of 800 at room temperature (RT) and 3000 at 3.8 K. RF characterization indicates a maximum f_T of 500 GHz at 3.8 K and 300 GHz at RT. The proposed figure-of-merit, ($g_m.f_T/I_c$), typically used in CMOS design, is explored across the temperature range. The study reveals a noise equivalent temperature of sub-1 K at 3.8 K with source matching. The noise behavior of Si/SiGe:C HBTs within 0.13 μm BiCMOS technology is characterized over 293 to 4 K and 10 kHz to 12 GHz. The analysis shows a significant increase in the flicker noise coefficient, K, and corner frequency reduction at 4 K. The high frequency parameter f_T reaches 500 GHz, demonstrating better performance compared to advanced CMOS nodes. This research supports the modeling of HBTs that are critical for circuits operating at cryogenic temperatures. These models are particularly beneficial for designing classical-to-quantum interfaces.

INDEX TERMS Low noise analysis, SiGe biCMOS technology, DC characterization, RF characterization, noise characterization, low-frequency noise, flicker noise coefficient, 1/f noise.

I. INTRODUCTION

Intensive research into cryogenic CMOS technology down to 16 nm nodes has been recently conducted over temperatures ranging from RT (293 K) to CT (4 K) [1]. These investigations have shown variations in multiple transistor parameters upon cooling. In the absence of cryogenic models, this research is vital for optimizing transistor performance, reducing tunable parameters, and thus improving design compactness and scalability. Cryo-CMOS technology has been shown to be effective in the read-out and control of quantum chips, specifically quantum bits or qubits, used in quantum computing. Additionally, heterojunction bipolar transistor (HBT) technology has exhibited its benefits, particularly because of its low 1/f noise and overall superior noise performance, making it advantageous for Low-Noise Amplifier (LNA) design. LNAs are the first active components interfacing with qubits or any superconducting detectors operating at CTs. Several studies have emphasized characterizing HBTs at temperatures down to 4 K, focusing on their DC, AC, and high-frequency noise performance [2]. However, low-frequency noise characterization is more challenging at both room and cryogenic temperatures due to the HBTs' extremely low noise levels, necessitating an optimally designed experimental setup to mitigate background noise. This research presents an in-depth analysis of an HBT fabricated using the SG13G2 0.13 μm Silicon Germanium (SiGe) BiCMOS process from IHP, now available as an open source Process Design Kit (PDK) [3]. Our study covers a broad temperature range, evaluating the Device Under Test's (DUT) DC, RF, and noise properties and introducing various design Figures-of-Merit (FoMs). These FoMs are particularly important in contexts where existing cryogenic models are limited or not fully validated, as they address critical aspects of power, speed, and gain. In Section II, we explore the DC

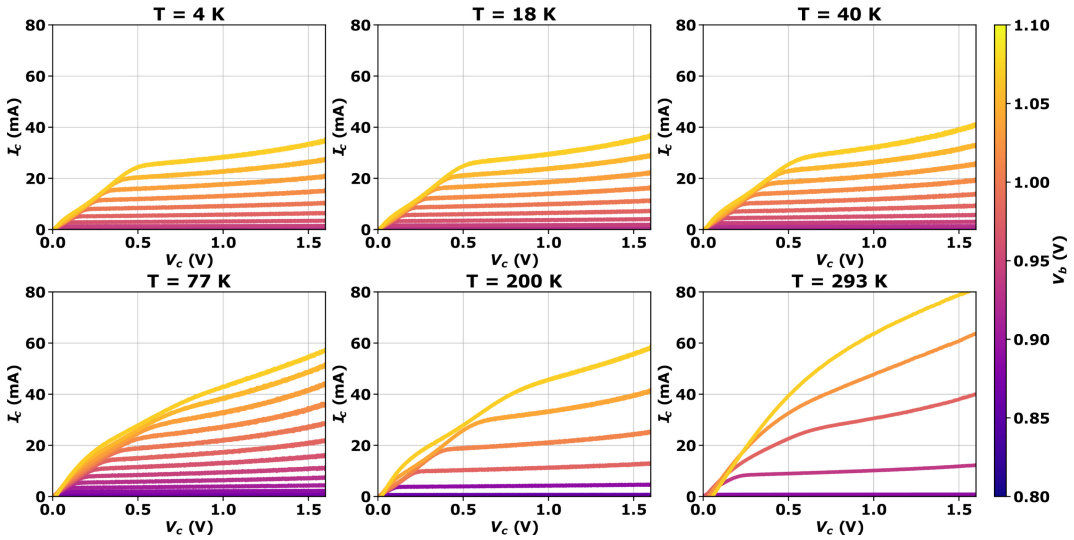

FIGURE 1. I_c-V_c plots at temperatures ranging from 293 to 4 K.

properties, essential for subsequent discussions and parameter extractions. Section III examines the factors influencing the performance of RF building blocks like LNAs, assessing the impact of these parameters across different temperatures and biases. Section IV provides a comprehensive analysis of the SiGe HBT DUT's noise characteristics over a wide temperature range (293 to 4 K) and frequency spectrum (10 kHz to 12 GHz). We investigated the noise properties of SiGe HBTs in relation to bias, frequency, and temperature. To the best of our knowledge, this is the first study to investigate low-frequency noise in SiGe HBTs across a broad temperature range, from 4 K to 293 K.

II. DC CHARACTERIZATION

A. GUMMEL PLOTS

In this section, we assess the performance of the terminal currents of the SiGe HBT DUT during the cooling process. To evaluate the collector current I_c and the base current I_b as a function of the base voltage V_b, we use two channels of the SDA B1500A [4] to force the collector and base voltages into the terminals. Both V_b and V_c are swept concurrently, maintaining a constant voltage difference of 0.1 V between the collector and the base. To avoid oscillations at the HBT output when the collector current is high, a wideband bias-tee integrated into the SDA [4] is used for both terminals, ensuring that the RF terminal of the bias-tee is connected to a 50 Ω load. The Gummel plots depict four distinct regions [5]:

Region 1: Ideal collector current: In this particular scenario, considering the dimensions of the device ($6 \times 0.07\,\mu m \times 0.9\,\mu m$), it can be presumed that the collector current primarily arises from the ballistic transport of minority carriers within the base and can be represented as:

$$J_c(T) = J_{c_0}(T) \cdot e^{qV_{be}/n_{c_0}kT}, \tag{1}$$

where J_{c_0} denotes the saturation collector current density, and n_{c_0} represents the ideality factor of the collector current under low-injection conditions [5]. At RT, n_{c0} is conventionally assigned a value of 1; this does not correspond to a physical parameter but rather indicates the level of ideality within the recombination current according to a forward-biased diode model, which assumes the current is due to a diffusion process. The parameter n_{c0} remains invariant with respect to bias, in contrast to n_c, which is bias-dependent and is defined as $I_c/g_m U_T$. At low injection levels, n_c converges to n_{c0}. The base current is predominantly affected by recombination events in the base region and can be modeled using the following diode equation:

$$J_b(T) = J_{b_{0,rc}}(T) \cdot e^{qV_{be}/n_{b_{rc}}kT}, \tag{2}$$

where $J_{b_{0,rc}}$ represents the saturation current density of the base recombination and $n_{b_{rc}}$ denotes the ideality factor associated with the base recombination current [6].

Region 2: Ideal collector and base currents: The collector and base currents exhibit ideal behavior within this specific portion of the Gummel plot. The mathematical representation of the collector current remains consistent with (1). In contrast, the base current now integrates three contributions: the ideal diffusion current, the recombination current (as in (2)), and a tunneling component, which becomes significant at cryogenic temperatures. This relationship is mathematically formulated as follows:

$$\begin{aligned} J_b(T) = {} & J_{b_0}(T) \cdot e^{qV_{be}/n_b kT} \\ & + J_{b_{0,rc}}(T) \cdot e^{qV_{be}/n_{b_{rc}}kT} \\ & + J_{b,\mathrm{tun}}(T), \end{aligned} \tag{3}$$

Here, the first term represents the ideal diffusion base current, the second term accounts for recombination current, and the third term $J_{b,tun}(T)$ denotes the tunneling base current component, as discussed in [7].

Region 3: Impact of access resistances (r_b, r_e): The collector and base currents do not follow an exponential

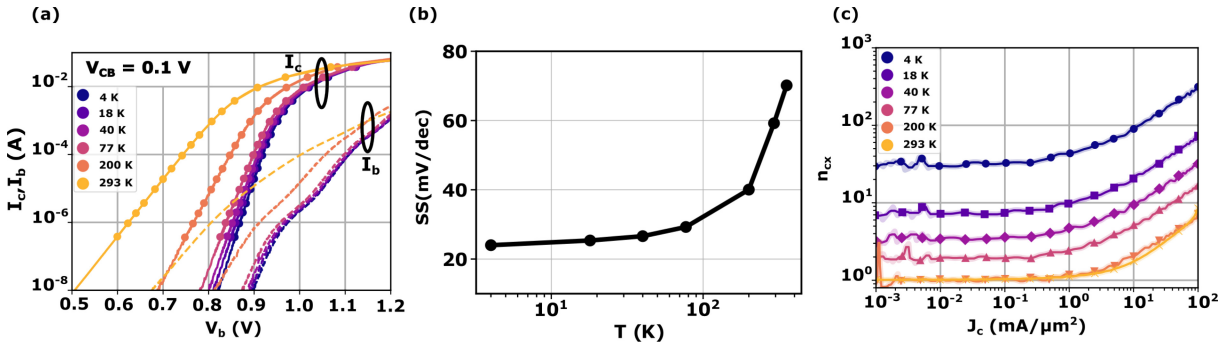

FIGURE 2. The DC characterization down to 4 K: (a) Gummel plots, (b) the subthreshold slope (SS) extraction, (c) n_{cx} extraction as function of J_c.

profile due to the considerable voltage drops across the base resistance r_b and the emitter resistance r_e at these current magnitudes. Hence, the V_{be} value is reduced at a given V_b, causing a minor deviation in the logarithmic relationship of I_c and I_b with V_b. In the forthcoming noise analysis section, the base resistance r_b will be analyzed by separating it into its external (bias-independent) and internal (bias-dependent) components. The emitter resistance r_e, which is primarily parasitic and not significantly bias-dependent, will also be discussed. The observed variation in total resistance with collector current will be clarified accordingly.

Region 4: High-injection regime: As the base and collector currents rise, the high injection effects become more significant. Fig 2(a) illustrates two primary effects. The first is the high injection current phenomenon, known as base push out or the Kirk effect [8]. The second effect is self-heating [9], [10], which adversely affects the device's performance, especially during high power and high-frequency operations. Fig 2(a) depicts the relationship between the collector and base currents with respect to the HBT base voltage over a temperature span of 293 to 4 K. Notably, data for voltages under 0.5 V are omitted from Fig. 2(a), as excessive noise rendered analysis impractical. Several insights emerge: firstly, as temperature lowers, the slope of the collector current versus base voltage becomes more pronounced, as demonstrated in Fig. 2(b). This denotes an enhancement in the subthreshold slope (SS), improving from 40 mV/dec at 293 K to 14 mV/dec at 4 K, resulting in a 65% increase. This enhancement is due to the rise in low-injection transconductance g_m with cooling. Additionally, it is observed that the base voltage V_b required for a given current increases during cooling, with a plateau occurring below 77 K, indicative of non-equilibrium transport phenomena. For a specified collector current density J_c and temperature T, the relationship can be expressed as:

$$n_{cx}(T, J_c) = \frac{J_c \cdot A_E}{g_{m_{eff}} \cdot U_T}, \tag{4}$$

where J_c denotes the collector current density, A_E specifies the emitter area, $G_{m_{eff}}$ represents the extrinsic transconductance, considering the emitter degeneration attributed to r_e, and is mathematically expressed as $g_m/(1 + g_m \cdot r_e)$. Lastly, U_T stands for the thermal voltage, defined as kT/q.

As shown in Fig. 3(c), decreasing the temperature of the HBT raises its threshold voltage due to the freezing of primary carriers in the emitter [11]. Concurrently, the current gain is enhanced because of the difference in band gap between the silicon emitter and the SiGe base. A significant 22% increase in the barrier potential V_{be_0} is observed, shifting from 0.8 V at 293 K to 0.98 V at 4 K [11]. This effect is beneficial for reducing leakage.

B. GAIN PERFORMANCE

At CT, SiGe HBTs show a significant increase in transconductance due to substantial band-gap changes and reduced thermal effects [12]. This improvement is particularly advantageous for SiGe LNAs, as demonstrated in [13]. However, operating at CTs introduces greater variability in device parameters, including transconductance, which is influenced by bandgap narrowing, mechanical stress, and germanium distribution [14]. The device transconductance is expressed as:

$$g_m = \frac{\partial I_c}{\partial V_{be}} \simeq \frac{qA_E J_c}{kT_{eff}}, \tag{5}$$

where T_{eff} represents the effective temperature of minority carriers and serves as a phenomenological parameter to model the impact of non-equilibrium transport, thereby clarifying the distribution behavior of minority carriers [15].

Using the previously discussed DD formalism, two significant alterations in the collector current with respect to the base voltage are expected as temperature decreases: Firstly, the increase in transconductance depicted in (5) leads to a steeper J_c-V_b curve at lower temperatures. Secondly, the curves shift rightward due to the decrease in intrinsic carrier concentration with falling temperature [2]. It is important to recognize that (5) is valid under the assumption that J_{c_0}, the saturation collector current density introduced in (1), remains bias-independent. At a current density J_c of 30 mA/μm^2, Fig. 4(a) demonstrates that the measured characteristics are not as steep as those predicted by the analytical DD model. The discrepancy between empirical data and standard DD theory at CT is primarily attributed to the initial assumption of bias dependence of various

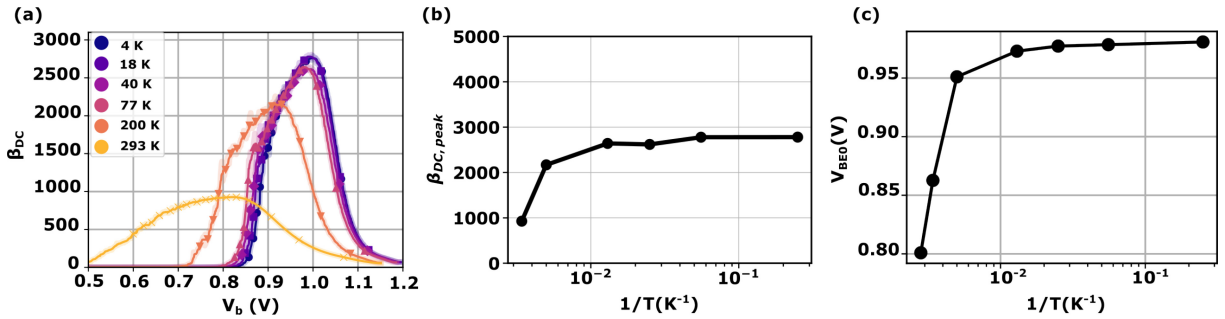

FIGURE 3. The extraction of the current gain β at 4: (a) as a function of the base voltage V_b, (b) the peak of β as a function of temperature, (c) V_{BE0} as a function of temperature.

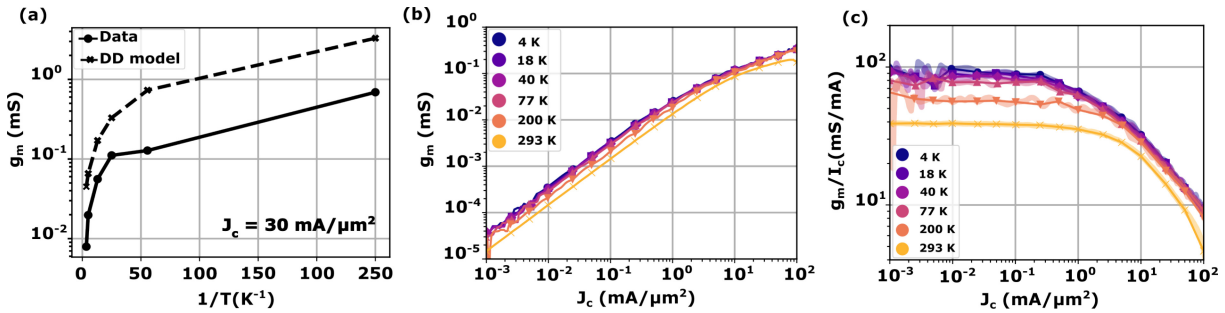

FIGURE 4. The extraction of the transconductance g_m: (a) the comparison of the DD model and the measured value, (b) as a function of J_c, (c) the FoM g_m/I_c as a function of J_c.

parameters, influenced by secondary phenomena such as neutral base recombination, carrier velocity saturation, and base width modulation. However, it is crucial to note that the trend of g_m with temperature remains consistent between the analytical model and the measurements.

C. GAIN-POWER FoM

For CMOS technology, the g_m/I_D methodology has emerged as a highly effective strategy for designing low-power analog circuits, even for the most advanced CMOS nodes [16]. However, there has been no investigation of the g_m/I_C FoM for SiGe HBTs, taking advantage of being insensitive to temperature. The objective of this section is to emphasize that optimizing power consumption and maximizing the HBT gain is important, maximizing the ratio g_m/I_c. The properties of the device in CT are affected by the enhancement of the high injection, the band edge, and the barrier effect [10]. These effects result in a premature decrease in both β and g_m at high J_c, and induce a rolloff that will be reflected in the g_m/I_c FoM. Consequently, as the temperature decreases, the bias margin becomes narrower. In the low-current injection regime, the introduced FoM can be expressed as:

$$\frac{g_m}{I_c} \simeq \frac{q}{kT_{eff}}. \tag{6}$$

The ratio of g_m to I_c, as illustrated by Equation (6), remains invariant under conditions of low current injection ($J_c \leq 0.1$ mA/μm^2 at 4 K and $J_c \leq 1$ mA/μm^2 at 293 K) for a given temperature T, and inversely correlates with it. This observation is supported by the data depicted in Fig. 4(c).

III. RF CHARACTERIZATION

A. MEASUREMENT SETUP

RF characterization was conducted using a closed-cycle helium probe station from Lakeshore [17]. In Fig. 6(a), high-frequency GSG probes are shown for RF and noise analysis addressed in the following section. The SDA B1500A provided bias voltage to the base and collector, with monitoring at various points during the sweeps. S-parameters were measured up to 12 GHz using a network analyzer (PNA-X N5245A, Keysight).

The SOLT (Short-Open-Load-Through) calibration method [18] was employed to eliminate effects up to the GSG pads of the DUT plane. On-chip fixtures, in both open and short configurations, were utilized to negate parasitic effects introduced by the die substrate and GSG pads. These procedures were repeated for each temperature to account for potential variations in parasitic values. Notably, the bias-tees integrated into the VNA in this setup exhibit a bandwidth of 40 GHz.

B. THE TRANSIT FREQUENCY f_T

The transit frequency (f_T) of an HBT is crucial in defining its efficiency at high frequencies. This critical parameter is influenced by the carrier transit time and the physical architecture of the device. An accurate f_T model requires the inclusion of these determinants. Enhancements in HBTs commonly aim to optimize transit times to achieve superior frequency performance [19]. f_T is correlated with the short-circuit current gain, which dissects the carrier transit times

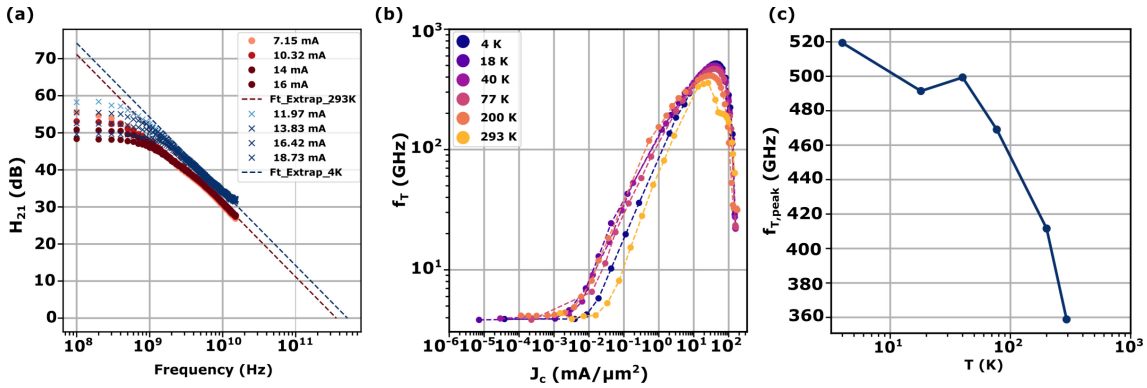

FIGURE 5. The transit frequency f_T extraction at 4 K: (a) the H-parameters extraction method, (b) the trend as a function of J_c, (c) the peak of f_T as function of temperature.

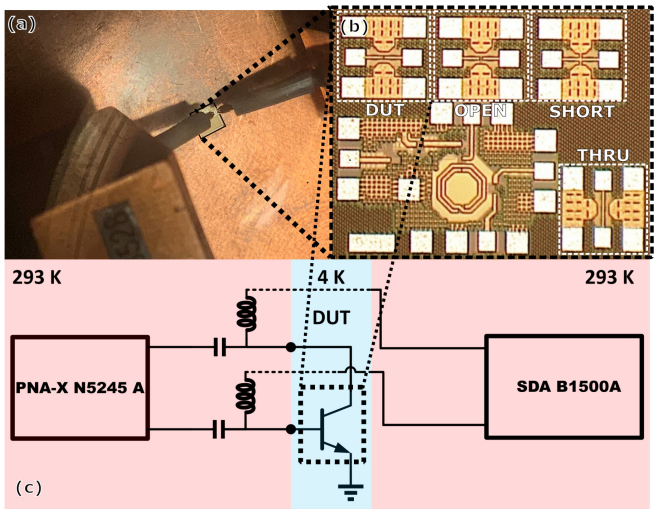

FIGURE 6. RF characterization setup: (a) Image of the chuck of the cryogenic probe station [17], (b) the Device Under Test (DUT), along with the open and short fixtures micrograph, (c) DC and RF test setup.

and the RC time constants to understand their influence on f_T and its limitations on the high-frequency capabilities [20]. By extrapolating from the de-embedded H-parameters illustrated in Fig. 5(a) with a 20 dB/dec slope, f_T can be evaluated. The point where $H_{21,dB}$ intersects the 0 dB line identifies f_T. The transit frequency is mathematically defined as:

$$f_T = \frac{1}{2\pi\,\tau_{EC}} = \frac{1}{2\pi\left(\frac{k\cdot T}{qI_c}\cdot(C_{be}+C_{bc}+C_p)\right)+\tau_B}. \quad (7)$$

In this context, τ_B denotes the transit time of minority carriers in the base, $U_T = kT/q$ is the thermal voltage, I_c indicates the collector current, and C_{be}, C_{bc}, and C_p represent the capacitances of the base-emitter junction, the base-collector junction, and the parasitic elements, respectively. Figure 5(b) illustrates the dependency of f_T on various collector current densities. When temperature decreases from 293 to 4 K, the optimal collector current density for achieving maximal speed increases, ranging from 10 to 80 mA/μm^2. Notably, the peak transit frequency rises from 350 GHz at 293 K with a current density of 10 mA/μm^2 to 510 GHz at 4 K under the same collector current density. Particularly, variations are subtler below 77 K, which is likely attributed to the maximum f_T occurring at high current densities, causing substantial self-heating. This finding consequently impacts the maximum achievable bandwidth of LNAs at 4 K.

C. MOBILITY ENHANCEMENT μ_e

Although the mobility of minority carriers is crucial for the performance of bipolar devices, there is a lack of studies dedicated to quantifying this parameter in SiGe HBTs at extremely low temperatures, such as 4 K. In this section, we share our experimental observations on the relationship between minority carrier mobility and temperature. In addition, we explore the influence of temperature on the recombination lifetime. The methodology for measuring minority carrier mobility follows the techniques described in [21]. In (7), τ_B is defined as in [21]:

$$\tau_B = \frac{q\cdot L_B^2}{kT\cdot\mu_e}. \quad (8)$$

The thickness of the base is denoted as L_B. Figure 7(a) presents the relationship between $1/f_T$ and $1/I_c$, where the Y-axis intercept correlates with the base transit time τ_B. This transit time is shown in Fig. 7(b). By employing (8), the mobility ratio relative to RT is inferred in Fig. 7(c). Detailed examination of the graphs in Fig. 7 indicates a notable 59% reduction in base transit time, which results in a 70% improvement in minority carrier mobility, as elaborated in [21]. These findings underscore the significant performance gains of SiGe HBTs, particularly at 4 K.

D. RF FoM

To enhance the power, speed, and gain of a DUT, a commonly used FoM in CMOS technology is $g_m\cdot f_T/I_D$ as suggested by [22]. We present an alternative methodology by investigating the temperature-dependent behavior of this FoM specifically for SiGe HBTs.

The results of the DC and RF analyzes highlight that to achieve maximum gain, it is beneficial to operate at

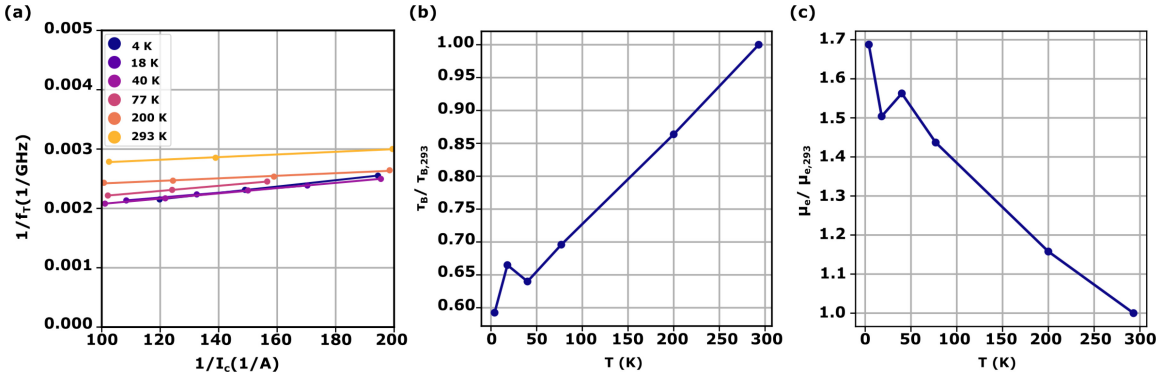

FIGURE 7. The mobility and base transit time of minority carriers down to 4 K, based on [21].

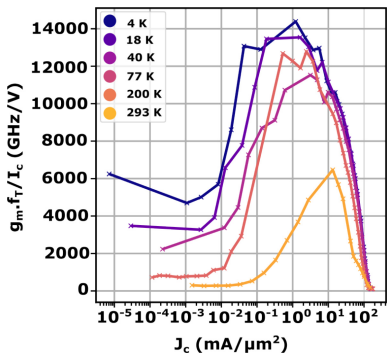

FIGURE 8. The extraction of $g_m.f_T/I_c$ FoM from 293 K down to 4 K.

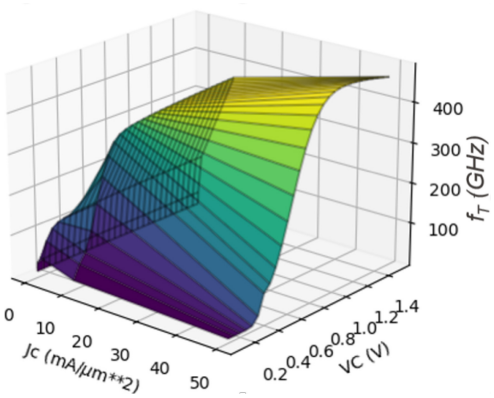

FIGURE 9. 3D representation of f_T as function of J_c and V_c at 4 K.

high injection levels. In contrast, for power efficiency while maintaining a designated gain, low to moderate injection levels are optimal at RT, shifting to deep-low injection levels at CT.

Fig. 9 presents a three-dimensional plot of the critical parameters: transit frequency f_T, collector voltage V_c, and collector current density J_c. The transit frequency f_T is indicative of the device's operational speed, J_c impacts its gain, and both V_c and J_c influence power consumption. Depending on the optimization objectives, designers can intuitively choose an appropriate analysis plane. To enhance the design process, the parameters are combined into FoM

TABLE 1. DC and RF summary table of the SiGe HBT performance.

Parameter	T = 293 K	T = 4 K	Temperature Dependence
DC Parameters			
β_{DC}	850	2750	224 % increase
V_{BE_0} (mV)	800	976	22 % increase
SS (mV/dec)	70	20	71 % decrease
Small Signal Model Parameters			
$\tau_B/\tau_{B,0}$	1	0.59	41 % decrease
$\mu_e/\mu_{e,0}$	1	1.7	70 % increase
$g_{m,peak}$ (mS)	189	350	85 % increase
RF Figures of Merit			
$f_{T,peak}$ (GHz)	350	520	49 % increase
$J_{c,opt}$ (mA/μm^2)	10	0.5	95 % decrease

$g_m \cdot f_T/I_c$, showing a significant improvement of 133%. Additionally, optimal performance shifts to the lower current injection range with decreasing temperature, as highlighted in Fig. 8.

IV. NOISE CHARACTERIZATION

Multiple studies have examined the electrical behavior of SiGe HBTs at CTs [14], [23], [24]. Nevertheless, key factors such as device self-heating, especially at elevated collector currents, and the cross-correlation between noise sources are often disregarded, with approximations frequently applied in noise characterization by isolating base resistance. This section explores the RF noise properties of SiGe HBTs, adjusting various parameters and temperatures from 293 to 4 K. The focus areas include operating frequency variations, collector current density J_c, and collector voltage V_c. Accurate noise models for HBTs which account noise correlation and thermal resistance are important for precise LNA design and simulation [25], [26]. This study is divided into two sections: the first section focuses on operating frequencies ranging from 100 MHz to 12 GHz, emphasizing the low noise figure of HBTs, while the second

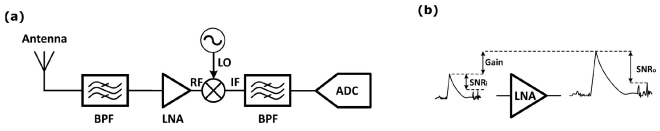

FIGURE 10. A conventional RF receiver architecture: (a) block diagram of the RX, (b) the LNA noise figure illustration.

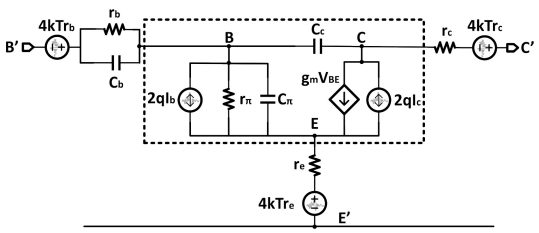

FIGURE 11. Complete small-signal HBT noise model.

section explores frequencies from 10 kHz to 1 MHz, highlighting the low-frequency noise benefits of this technology compared to CMOS [27], [28].

A. HIGH-FREQUENCY NOISE

A.1. INPUT NOISE CURRENT AND NOISE VOLTAGE IN SIGE HBTs

According to [15], the formulations for the power spectral densities of the input noise current S_{i_n}, the input noise voltage S_{v_n}, and their cross-correlation $S_{i_n v_n *}$ are presented as follows:

$$\begin{cases} S_{i_n} &= 2q\frac{I_c}{\beta} + \frac{2qI_c}{|\frac{Y_{21}}{Y_{11}}|^2}, \\ S_{v_n} &= 4kTr_b + \frac{2qI_c}{|Y_{21}|^2}, \\ S_{i_n v_n *} &= \frac{2qI_c Y_{11}}{|Y_{21}|^2}. \end{cases} \tag{9}$$

The simplified noise model for the HBT enables us to express the Y-parameters based on the primary characteristics of the device. Given that the operation occurs at frequencies below the transistor's unity current gain frequency (f_T), the power spectral densities of the input noise current S_{i_n} can be outlined as follows:

$$S_{in} = 2qI_c\left[\frac{1}{\beta} + \frac{1}{\beta^2} + \left(\frac{f}{f_T}\right)^2\right]. \tag{10}$$

According to (9), conducting a comprehensive noise analysis necessitates the determination of two fundamental parameters: base resistance (r_b) and emitter resistance (r_e).

A.2. EMITTER RESISTANCE r_e

The effect of emitter resistance r_e on the high-frequency performance of HBTs cannot be disregarded [29]. This influence amplifies with the reduction in the emitter size [30], resulting in transistor degeneration. Multiple investigations have been undertaken to determine this parameter, either via device characterization and estimation with a basic small-signal model, or through the measurement of sheet resistance and emitter area [31]. Nevertheless, it has been observed

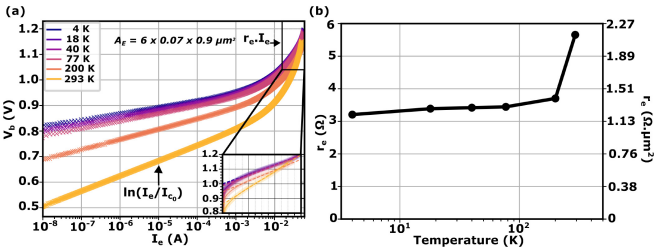

FIGURE 12. Extraction of the emitter resistance r_e at different temperatures using linear fit at high emitter current I_e.

that r_e for HBTs cannot be accurately derived from test structures, unlike other small-signal parameters [32]. In our study, because of the unknown temperature dependence of the sheet resistance, we propose a parameter-based extraction method based on collector impact ionization. Specifically, as demonstrated in [32], the equation incorporating r_e is:

$$V_b = r_e \cdot I_e + n_b V_T ln\left(\frac{I_e}{I_{c0}}\right), \tag{11}$$

where $n_b V_T$ and I_{c0} remain constant at a specified temperature. The findings in Fig. 12 indicate a roughly 45% drop in the emitter's resistance when the temperature is reduced from 293 K to 200 K. However, no significant further reduction is observed at 4 K. The emitter resistance consists of two parts: the external polyemitter and the intrinsic emitter. According to [2], the aforementioned reduction predominantly impacts the external polyemitter's resistance.

A.3. BASE RESISTANCE r_b

The second parameter crucial for extraction is the base resistance r_b, which significantly influences the device's noise characteristics and power gain. It reduces input power and adds to the thermal noise at the base terminal. Thus, minimizing base resistance is essential, though challenging in both fabrication and design. The base resistance is composed of two parts: the intrinsic base resistance, which is current-dependent, and the contact resistance, which remains constant regardless of bias conditions.

In this section, we employ the "circle impedance" method to determine the base resistance [33]. This involves short-circuiting the output port and measuring the input impedance, which is equal to h_{11}. This approach assumes the emitter resistance r_e is negligible compared to r_b. Nonetheless, it is crucial to acknowledge that this assumption has its limitations, as it might lead to an overestimation of the thermal noise from the base. Assuming this condition holds, the real and imaginary parts of h_{11} can be described as follows [15]:

$$\begin{cases} x = \Re(h_{11}) = (r_b + r_e) + \frac{g_{be}}{g_{be}^2 + (\omega C_i)^2}, \\ y = \Im(h_{11}) = -\frac{\omega C_i}{g_{be}^2 + (\omega C_i)^2}. \end{cases} \tag{12}$$

The intrinsic capacitance, C_i, is characterized by the relation $\omega C_i = g_m \cdot f/f_T$. The equation (12) can be expressed

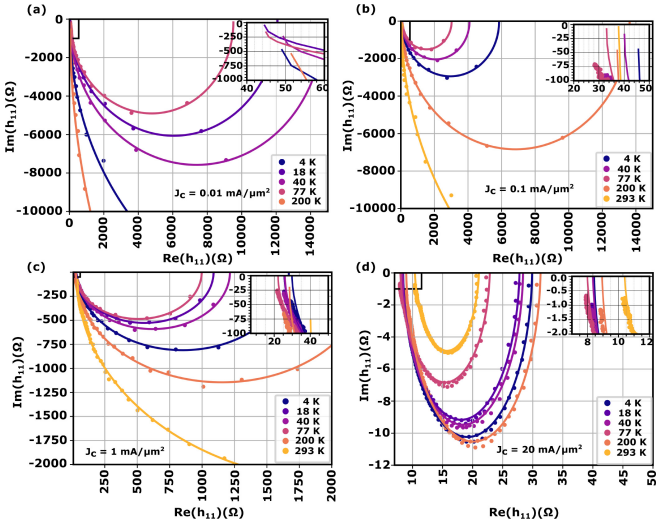

FIGURE 13. Base resistance (r_b) extraction using the semi-circle fitting method with h_{11} for three distinct current densities: (a) $J_c = 0.01$ mA/μm^2, (b) $J_c = 0.1$ mA/μm^2, (c) $J_c = 1$ mA/μm^2, and (d) $J_c = 20$ mA/μm^2.

as a circle equation, centered at $(r_b + 1/g_{be_0})$ with a radius of $1/2g_{be}$. The intersection of the fitted impedance circle with the real axis reveals the base resistance [15]. Notably, the h_{11} data was collected within the frequency range of 100 MHz to 12 GHz.

The results shown in Fig. 13 illustrate that in low injection regimes, particularly at $J_c = 0.01$ mA/μm^2, the semicircle model and the data points diverge at high frequencies. This deviation in the fitting curve introduces errors when estimating noise characteristics at these low injection levels. However, in moderate and high injection regimes, the measured data points (dots) and the semi-circle equation (solid circles) fit well. By extracting r_e and r_b across various collector current densities and temperatures, it is possible to derive different noise parameters starting with the noise figure (or its equivalent noise temperature).

A.4. THE MINIMUM NOISE TEMPERATURE T_{min}

The noise figure is a useful metric for gauging the amount of noise introduced by the amplifier and acts as an indicator of the minimum detectable signal.[1] Specifically, for a two-port network, the noise factor F can be expressed as [2]:

$$NF = NF_{min} + \frac{R_n \mid Y_s - Y_{s,opt} \mid^2}{\Re\{Y_s\}}, \tag{13}$$

NF_{min} being the minimum noise figure, and R_n stands for the noise resistance. This resistance is essential for assessing the sensitivity of the noise figure to variations from the optimal source admittance, labeled $Y_{s,opt}$. The expression for NF_{min}

[1]This section often uses the terms noise figure and noise factor interchangeably, which are related by the equation NF = 10·log(F).

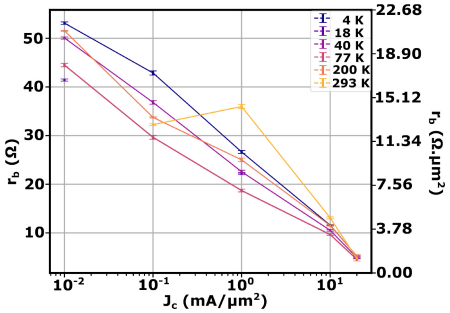

FIGURE 14. $r_b + r_e$ extraction using the h_{11} semicircle fitting method for different collector current densities.

can be derived as a function of the noise spectral densities, the optimum source admittance, and noise resistance R_n as:

$$\begin{cases} NF_{min} = 1 + 2R_n\left(G_{s,opt} + \frac{\Re(S_{in v_n *})}{S_{v_n}}\right), \\ NF_{min,an} = 1 + \frac{1}{\beta} + \sqrt{\frac{2g_m(r_b + r_e)}{n_c}}\sqrt{\frac{1}{\beta} + \left(\frac{f}{f_T}\right)^2}. \end{cases} \tag{14}$$

where $\Re$ represents the real part of a parameter. In the common scenario where $g_m r_b \gg 1/2$, and by expressing the noise spectral densities S_{in}, S_{v_n}, and $S_{in v_n *}$ in terms of the device parameters r_b, β, I_c, and f_T, NF_{min} can be approximated to $NF_{min,an}$ as shown in (14) [15]. This equation illustrates that NF_{min} increases consistently with frequency. However, distinct behaviors can be observed based on the relationship between the operating frequency f and f_T.

- $f \ll f_T/\sqrt{\beta}$: The first term $(1/\sqrt{\beta})$ in the square root expression is dominant, leading to white-noise behavior.
- $f \gg f_T/\sqrt{\beta}$: The second term dominates, causing a −10 dB/decade increase.
- $f = f_T/\sqrt{\beta}$: This frequency, marked as f_0, serves as a critical point in the expression for the minimum noise figure, indicating a transition from frequency-independent white noise to a 10 dB/decade rise as frequency increases.

NF_{min} rises consistently with the current through g_m, irrespective of frequency behavior. Nonetheless, there are three methods to reduce NF_{min} at a specific frequency f:

- *Increase the current gain* β
- *Increase the transit frequency* f_T
- *Reduce the base resistance* r_b

The first two methods become practical as the temperature drops, as discussed in the preceding sections. However, for the third method, r_b increases as the temperature decreases, as illustrated in Fig. 14. Therefore, it is essential to focus on minimizing the product $g_m \cdot r_b$. For evaluating noise at CT, noise temperature (T_n) is generally preferred over noise figure. This parameter assesses system noise by equating it to an equivalent temperature. It is crucial to recognize that noise temperature does not reflect the actual physical temperature of the system. Instead, it signifies a theoretical value indicating the temperature required to produce a

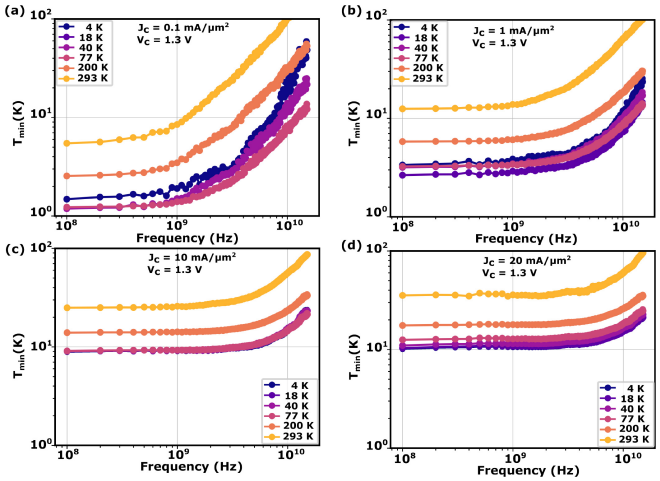

FIGURE 15. The extraction of the minimum noise temperature (T_{min}) using equation (14) as a function of frequency for three different collector current densities: (a) $J_c = 0.1$ mA/μm^2, (b) $J_c = 1$ mA/μm^2, (c) $J_c = 10$ mA/μm^2, and (d) $J_c = 20$ mA/μm^2.

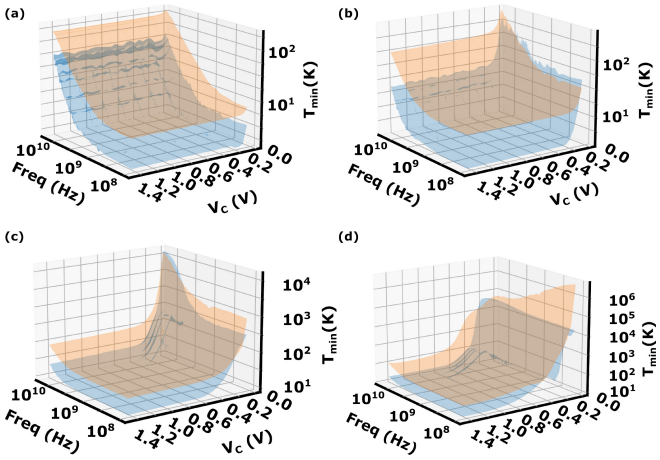

FIGURE 16. 3D visualization of the minimum noise temperature (T_{min}) as a function of both frequency and the collector voltage V_c for three distinct collector current densities: (a) $J_c = 0.1$ mA/μm^2, (b) $J_c = 1$ mA/μm^2, (c) $J_c = 10$ mA/μm^2, and (d) $J_c = 20$ mA/μm^2.

specific quantity of thermal noise power per unit bandwidth within the system [34]. The noise temperature T_n of a two-port network is defined as [2]:

$$T_n = T_{min} + T_0 \frac{R_n \mid Y_s - Y_{s,opt} \mid^2}{\Re\{Y_s\}}, \tag{15}$$

where $T_{\min}$ represents the minimum equivalent noise temperature, R_n denotes the noise resistance, and Y_s indicates the source admittance. The equation below establishes the relationship between the noise figure and the equivalent noise temperature:

$$NF = 10 \cdot log\left(\frac{T_n}{T_{ref}} + 1\right), \tag{16}$$

where T_{ref} is set to 290 K unless stated otherwise. The procedure used to reduce NF_{min} can also be applied to optimizing T_{min}.

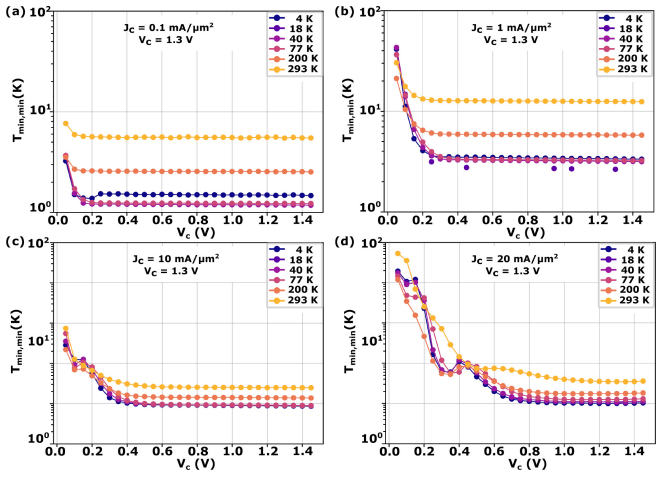

FIGURE 17. The extraction of the global minima of (T_{min}) across the frequency range as a function of the collector voltage V_c for three distinct current densities: (a) $J_c = 0.1$ mA/μm^2, (b) $J_c = 1$ mA/μm^2, (c) $J_c = 10$ mA/μm^2, and (d) $J_c = 20$ mA/μm^2.

A.5. NOISE RESISTANCE R_n

In cases requiring noise matching to enhance HBT noise performance, the noise figure condition $NF = NF_{min}$ is typically fulfilled by matching the input admittance Y_s to the optimal admittance $Y_{s,opt}$, as will be detailed in the subsequent section. Conversely, for gain matching scenarios aiming at maximum power transfer, the input admittance should match the value $Y_{s,gain} = 1/Z_0$, with Z_0 conventionally set to 50 Ω to align with standard high-frequency cables and minimize reflection losses. Notably, a design's efficiency improves if $Y_{s,opt}$ and $Y_{s,gain}$ overlap, facilitating a common source admittance Y_s for both noise and power matching conditions. The variance between these admittances is identified as the optimum reflection coefficient Γ_{opt}, which is defined as:

$$\Gamma_{opt} = \frac{1 - Y_{s,opt}Z_0}{1 + Y_{s,opt}Z_0}. \tag{17}$$

Equation (13) demonstrates that a minimized R_n is advantageous when the source is deliberately terminated at a value distinct from $Y_{s,opt}$. According to the noisy two-port linear theory [35], at an ambient temperature T_a, the noise resistance R_n can be formulated as:

$$R_n = \frac{S_{v_n}}{4kT} \simeq \frac{T_a}{T_{ref}}\left(r_b + r_e + \frac{n_c}{2g_m}\right). \tag{18}$$

The ideality factor for the collector current, denoted as $n_c = \frac{I_c}{g_m V_T}$, is extracted as shown in Fig. 2(c). At high current densities, as clarified in the base resistance extraction section, $r_b + r_e$ remains unaffected by temperature fluctuations, thereby remaining constant for transconductance g_m. Conversely, n_{cx} increases by a factor of 20. Irrespective of the operating frequency, the resistance R_n defines the noise figure (NF) sensitivity to deviations at the source termination $Y_{s,opt}$. A reduced value of $r_b + r_e$ aids in maintaining the NF near its minimum value ($NF_{\min}$) when the source impedance

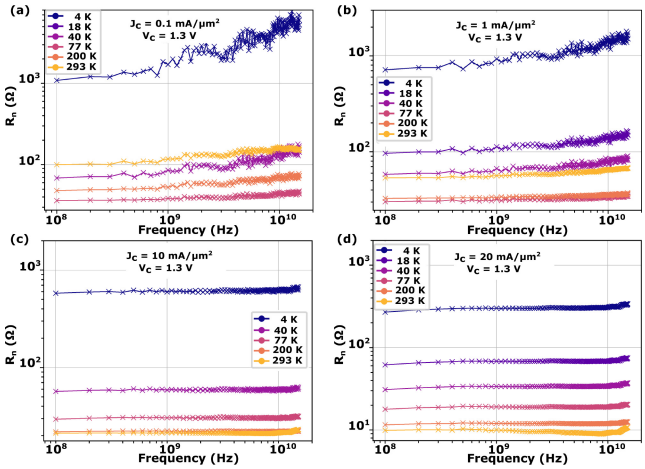

FIGURE 18. The extraction of the noise resistance (R_n) using equation (18) for three different collector current densities: (a) $J_c = 0.1$ mA/μm^2, (b) $J_c = 1$ mA/μm^2, (c) $J_c = 10$ mA/μm^2, and (d) $J_c = 20$ mA/μm^2.

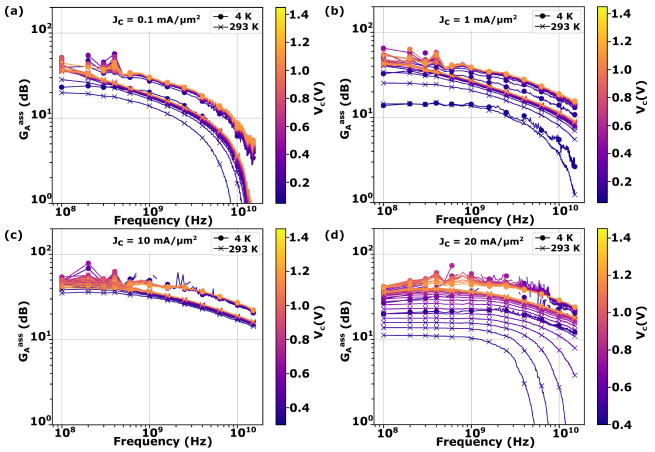

FIGURE 19. The extraction of the associated gain G_a^{ass} using equation (21) as a function of both frequency and the collector voltage V_c for three distinct current densities: (a) $J_c = 0.1$ mA/μm^2, (b) $J_c = 1$ mA/μm^2, (c) $J_c = 10$ mA/μm^2, and (d) $J_c = 20$ mA/μm^2.

is matched rather than optimized for noise. It is important to emphasize that R_n scales directly with the size of the device, while $Y_{s,opt}$ scales inversely. Thus, the values shown in Fig. 18 are for the present size DUT, which measures $6 \times 0.07\,\mu m \times 0.9\,\mu m$.

A.6. OPTIMUM SOURCE ADMITTANCE $Y_{s,opt}$

The optimum source admittance, represented by $Y_{s,opt} = G_{s,opt} + jB_{s,opt}$, is made up of a real part, $G_{s,opt}$, and an imaginary part, $B_{s,opt}$. Both elements can be expressed as functions that depend on the noise spectral densities mentioned earlier in this section:

$$\begin{cases} G_{s,opt} = \sqrt{\dfrac{S_{in}}{S_{vn}} - \left[\dfrac{\Im(S_{in v n*})}{S_{vn}}\right]^2} \\ B_{s,opt} = -\dfrac{\Im(S_{in v n*})}{S_{vn}}. \end{cases} \tag{19}$$

Equation (20) allows for simplification of the given expressions. In particular, the optimized expression for $B_{s,opt}$ implies the necessity of a series inductor at the input to cancel out the imaginary part:

$$\begin{cases} G_{s,opt,an} = \sqrt{\dfrac{g_m}{2R_n}\dfrac{1}{\beta} + \dfrac{g_m (f/f_T)^2}{2R_n}\left(1 - \dfrac{1}{2g_m R_n}\right)} \\ B_{s,opt,an} = -\dfrac{f}{2R_n f_T}. \end{cases} \tag{20}$$

A.7. THE ASSOCIATED GAIN G_a^{ass}

The associated gain, denoted G_a^{ass}, is dependent on the degree to which the noise-matching and gain-matching conditions are met [15]. This gain represents the highest achievable gain when the source termination (Y_s) meets the optimal noise matching condition ($Y_{s,opt}$). Designers aim for a high value of this parameter, as it is ideal for it to align closely with the gain-matching condition. An amplifier's effectiveness is compromised if it has a low noise figure but insufficient gain. However, realizing this objective is challenging in practical scenarios at both the device and circuit levels. The associated gain (G_a^{ass}) can be mathematically expressed through various small signal parameters [36]:

$$\begin{cases} G_a^{ass} = \dfrac{1}{\omega^2 C_{bc} C_i r_b} \cdot \dfrac{\kappa}{\sqrt{2}}, \\ \kappa = \sqrt{\dfrac{1+2g_m(r_b+r_e)}{n_c} \cdot \dfrac{g_m^2}{\beta} + \dfrac{g_m(r_b+r_e)}{n_c} \cdot (\omega C_i)^2}. \end{cases} \tag{21}$$

Equation (21) reveals that the associated gain (G_a^{ass}) rises with increasing collector current (I_c), primarily due to the g_m component, which necessitates a certain I_c level to achieve a satisfactory associated gain. Conversely, an increase in the transistor's current gain (β) leads to a reduction in G_a^{ass}, as suggested by the leading term inside the square root. This implies that any reduction in noise figure due to increased β results in diminished associated gain. The influence of β on G_a^{ass} is more prominent at lower frequencies, diminishing at higher frequencies. Moreover, G_a^{ass} decreases as frequency rises; at lower frequencies, the leading term within the square root prevails, exhibiting a frequency dependence of nearly $\frac{1}{\omega^2}$ (i.e., –20 dB/decade), whereas at higher frequencies, the subsequent term dominates, showing a frequency dependence close to $1/\omega$ (i.e., –10 dB/decade). The analysis of the equation indicates that the two terms equalize at $f = f_T/\sqrt{\beta}$. A shorter transit time (higher f_T) is preferable to enhance G_a^{ass} due to a smaller C_i, aligning with standard device design practices for noise reduction. Additionally, minimizing the C_{bc} capacitance is beneficial to improve G_a^{ass}, which is also crucial for achieving higher f_{max}. Figure 19 demonstrates the determination of G_a^{ass} based on (21), depicting its dependency on frequency and collector voltage V_c across four current densities: $J_c = 0.01$ mA/μm^2, $J_c = 0.1$ mA/μm^2, $J_c = 1$ mA/μm^2, and $J_c = 20$ mA/μm^2. Furthermore, Fig. 20 offers a 3D visualization to determine the minimum V_c necessary to sustain a satisfactory G_a^{ass} for reduced power consumption. Similarly, Fig. 17 shows T_{min} behavior, while Fig. 16 provides a 3D representation to

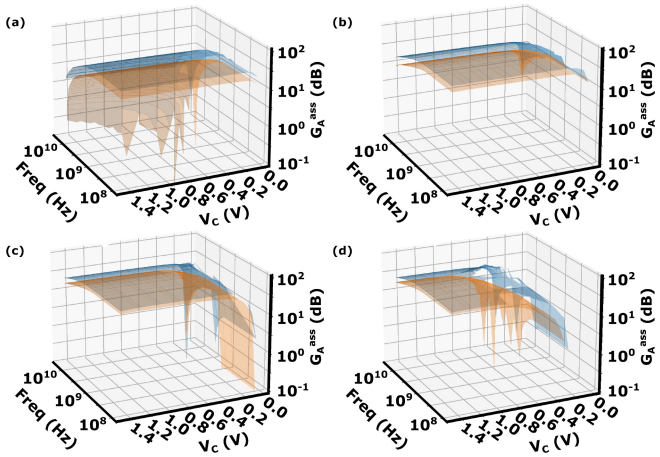

FIGURE 20. 3D visualization of the associated gain G_a^{ass} as a function of both frequency and the collector voltage V_c for three distinct current densities: (a) $J_c = 0.1$ mA/μm^2, (b) $J_c = 1$ mA/μm^2, (c) $J_c = 10$ mA/μm^2, and (d) $J_c = 20$ mA/μm^2.

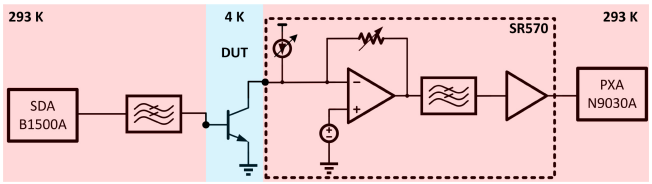

FIGURE 21. Low-frequency noise characterization setup.

facilitate the extraction of optimal operating points at various temperatures.

B. LOW-FREQUENCY NOISE

In SiGe HBTs, the low-frequency noise levels are comparable to those in Si BJTs and significantly lower than in III-V HBTs [37]. Both the base and collector currents exhibit low-frequency noise, with the base current 1/f noise typically being more dominant. The base current 1/f noise can be indirectly measured through collector noise voltage or directly at the base. Methods exist for simultaneous measurement of base and collector low-frequency noises and their coherence, often utilizing equivalent circuits to identify internal noise sources from collected data. However, conventional equivalent circuit models may produce unrealistic outcomes for high-speed SiGe HBTs operating at high current densities due to effects like self-heating.

In CTs, RF designs like VCOs [38], mixers [39], and LNAs [13] are crucial for qubit control. Although SiGe HBTs exhibit advantageous noise performance, there is a lack in low-frequency noise analysis for this technology at temperatures as low as 4 K. The following study provides a comprehensive characterization of low-frequency noise in SiGe HBTs down to 4 K, facilitating the development of enhanced VCOs and complete RF receivers in SiGe BiCMOS technology. It is important to recognize that this study represents the initial documentation of 1/f noise findings for SiGe HBT down to 4 K.

B.1. MEASUREMENT SETUP

Conducting measurements of low-frequency noise presents significant difficulties, primarily due to the minimal noise current at the base of the HBT. To overcome this issue, our methodology mirrored the configuration used to characterize flicker noise at RT [40]. As depicted in Fig. 21, a precise source measurement unit [4] (Keysight SDA B1500A) supplies the base voltage V_b, which is filtered to eliminate line noise interference. A current pre-amplifier [41] (Keysight SR570) provides the collector voltage V_c and amplifies the collector current, incorporating the base's amplified noise. The spectrum analyzer [42] (Keysight PXA N9030A) allows the analysis of the collector current in the frequency domain, resulting in the low-frequency noise plots that will be presented. The DUT was probed using ground-signal-ground (GSG) probes. The conversion from dBm to A^2/Hz using the signal analyzer is expressed as follows [43]:

$$S_{i_c} = 10^{\frac{x}{10}} \cdot 10^{-3} \cdot \frac{R_0}{K \cdot RBW \cdot R_a^2}\left[A^2/Hz\right], \tag{22}$$

In (22), the variable x represents the dBm value recorded by the PXA. RBW refers to the resolution bandwidth of the PXA, and K denotes the conversion factor for RBW, which is assumed to be 1. R_0 indicates the output impedance of the PXA, valued at 50 Ω, while R_a represents the transimpedance gain of the SR570 [41]. The next phase entails transforming S_{i_c} to S_{i_b} by taking into account the HBT current gain β.

B.2. FLICKER NOISE MODELING

MOS transistors are known for generating higher levels of flicker noise relative to bipolar transistors. The observed $1/f^3$ phase noise arises from the up-conversion of this flicker noise, making it highly prevalent in CMOS oscillators [44], [45], [46], [47], [48]. In [45], simulations illustrate that the phase noise driven by low-frequency flicker noise follows a $1/f^3$ dependence on the offset frequency. These simulation results are in congruence with experimental data available in the literature, substantiating the correlation between flicker noise and phase noise in CMOS oscillators. It is noteworthy that the flicker noise does not adhere strictly to the $1/f^3$ phase noise corner but is influenced by the VCO's design quality. The power spectral density of the noise current at the HBT base, S_{i_b}, can be defined as [15]:

$$S_{i_b}(i_b, f) = K_{F_T} \cdot \frac{i_b^{\alpha_T}}{f^{\gamma_T}}, \tag{23}$$

The parameter α_T clarifies the primary origin of low-frequency noise, whereas β_T characterizes the attenuation rate of noise across frequencies and is assessed at low frequencies corresponding to various collector current densities, denoted as J_c. At a temperature of 4 K, the linear fit of the low-frequency spectrum reveals α_4 to be approximately 1.61 and γ_4 to be around 2. Likewise, at 293 K, α_{293} is close to 1.86 and γ_{293} about 1.85. These extracted values provide deeper insights into the dominant noise mechanisms: the value of α_{293} approaching 2 at RT strongly suggests

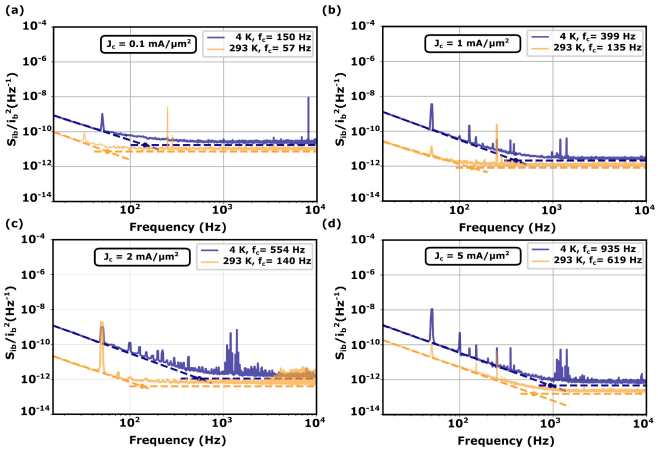

FIGURE 22. Normalized noise spectral density (S_{ib}) from 10 Hz to 10 kHz both at 293 and 4 K for four different collector current densities: (a) J_c = 0.1 mA/μm^2, (b) J_c = 1 mA/μm^2, (c) J_c = 2 mA/μm^2, and (d) J_c = 5 mA/μm^2.

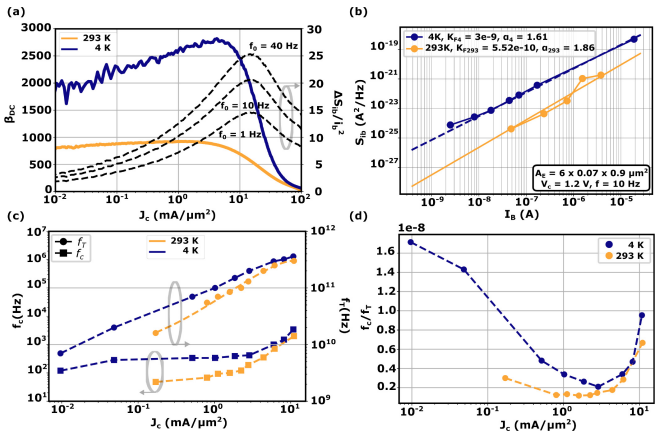

FIGURE 23. The extraction of the SiGe HBT noise characteristics down to 4 K: (a) the relative change of the normalized noise spectral density (S_{ib}) at different frequencies f_0, (b) K_F extraction curve, (c), (d) f_c/f_T FoM extraction down to 4 K.

the noise primarily arises from carrier number fluctuations (McWhorter-type model), consistent with recombination and trapping/detrapping phenomena at heterointerfaces or bulk defects. Conversely, the lower value of α_4 at CTs (4 K) indicates a mixed contribution, where both carrier number and mobility fluctuation (Hooge-type) mechanisms significantly influence the noise characteristics. Such a shift in dominant mechanisms at low temperatures aligns well with the diagnostic methodologies outlined in [49].

The relative change in S_{i_b}/i_b^2 at a specific frequency f_0, when transitioning from 293 K to 4 K, can be represented as:

$$\frac{S_{i_b}/i_b^2}{S_{i_b}/i_b^2}(i_c) = \frac{K_{F_4}}{K_{F_{293}}} \cdot f_0^{\Delta\gamma} \cdot \frac{\beta_{293}^{\alpha_{293}}}{\beta_4^{\alpha_4}}(i_c) \cdot i_c^{\Delta\alpha}, \tag{24}$$

where $\Delta\alpha$ is determined as $|\alpha_{293} - \alpha_4|$, and $\Delta\gamma$ is similarly defined. The corner frequency is calculated using the following equation:

$$\begin{cases} S_{i_b}(i_b, f_c) = 2qi_b \\ f_c = \left(\frac{K_{F_T}}{2q}\right)^{\frac{1}{\gamma_T}} \cdot I_B^{\frac{\alpha_T - 1}{\gamma_T}}, \end{cases} \tag{25}$$

where K_{F_T} is the flicker noise coefficient of the HBT at a temperature T.

When developing RF components like Voltage-Controlled Oscillators (VCOs), assessing just the corner frequency f_c proves inadequate for a comprehensive evaluation of a technology's capabilities. This is due to the omission of the frequency response attributes. SiGe HBTs exhibit a high f_T that peaks at 500 GHz at a temperature of 4 K, along with a low corner frequency, as depicted in Fig. 23(d). This underscores the technological benefits of SiGe HBTs when contrasted with CMOS technologies, as demonstrated by the introduced Figure of Merit (FoM) [15]. Nevertheless, a precise determination of this FoM's variation at 4 K mandates a thorough analysis, which is detailed in Fig. 22(d), showing the FoM f_c/f_T plotted against various collector current densities J_c at both 4 K and 293 K. While this work focuses on empirical characterization of flicker noise across temperature and bias conditions, future studies could further analyze the origin of the 1/f noise by distinguishing between mobility fluctuation (Hooge) [50] and carrier number fluctuation (McWhorter) models [51], which would provide deeper insight into the underlying noise mechanisms.

V. CONCLUSION

This paper presents a unified and comprehensive analysis of the DC,RF and noise performance of advanced Si/SiGe:C HBTs fabricated in a 0.13 μm BiCMOS platform, spanning a temperature range from 293 K down to 4 K and frequencies from 10 kHz to 12 GHz. While individual aspects of HBT behavior have been studied in previous works, this is the first report to combine both low-frequency and high-frequency noise characterization down to cryogenic temperatures in a single, coherent study. Our findings confirm that SiGe HBTs achieve excellent performance at 4 K, with a transit frequency reaching 500 GHz and current gain up to 3000, making them highly suitable for cryogenic LNAs, VCOs, and other quantum interface circuits. Furthermore, we propose a set of novel 2D and 3D design-oriented plots that link noise behavior with power consumption, speed, and gain—providing a practical toolset for designers working in temperature-constrained environments where current compact models remain limited. This work contributes new benchmarking data, fills a critical gap in low-temperature noise modeling, and provides actionable insights for RF design at cryogenic temperatures. As such, it offers both scientific value and practical relevance, and we believe it represents a novel and citable contribution to the field of cryogenic RF and quantum interface circuit design.

REFERENCES

[1] H.-C. Han, F. Jazaeri, A. D'Amico, A. Baschirotto, E. Charbon, and C. Enz, "Cryogenic characterization of 16 nm FinFET technology for quantum computing," in *Proc. IEEE 47th Eur. Solid State Circuits Conf. (ESSCIRC)*, 2021, pp. 71–74.

[2] J. C. Bardin, "Silicon-germanium heterojunction bipolar transistors for extremely low-noise applications," Ph.D. dissertation, Dept. Elect. Eng., California Inst. Technol., Pasadena, CA, USA, 2009.

[3] K. Herman et al., "On the versatility of the IHP BiCMOS open source and manufacturable PDK: A step towards the future where anybody can design and build a chip," *IEEE Solid-State Circuits Mag.*, vol. 16, no. 2, pp. 30–38, Jul. 2024.

[4] "B1500A semiconductor device analyzer Datasheet," Datasheet, Keysight, Santa Rosa, CA, USA, 2023. [Online]. Available: https://www.keysight.com/us/en/assets/9018-01850/user-manuals/9018-01850.pdf

[5] J. Bardin, S. Montazeri, and S.-W. Chang, "Silicon germanium cryogenic low noise amplifiers," in *Proc. J. Phys. Conf. Ser.*, vol. 834, 2017, Art. no. 12007.

[6] D. Knoll et al., "Base currents of Si/SiGe/Si HBT in dependence on the processing conditions," *Appl. Surf. Sci.*, vol. 102, pp. 247–251, Aug. 1996.

[7] M. Schröter and X. Jin, "A physics-based analytical formulation for the tunneling current through the base of bipolar transistors operating at cryogenic temperatures," *IEEE Trans. Electron Devices*, vol. 70, no. 1, pp. 247–253, Jan. 2023.

[8] P. Mushini and K. Roenker, "Simulation study of high injection effects and parasitic barrier formation in SiGe HBTs operating at high current densities," *Solid-state Electron.*, vol. 44, pp. 2239–2246, Dec. 2000.

[9] S. Mcalister, W. Mckinnon, S. Kovacic, and H. Lafontaine, "Self-heating in multi-emitter SiGe HBTs," *Solid-State Electron.*, vol. 48, nos. 10–11, pp. 2001–2006, 2004.

[10] R. Sampathkumaran and K. Roenker, "Effects of self-heating on the microwave performance of SiGe HBTs," *Solid-State Electron.*, vol. 49, pp. 1292–1296, Aug. 2005.

[11] A. A. Cherepanov, I. Novikov, and V. Vasiliev, "An evaluation of SiGe HBT operation at cryogenic temperatures," in *Proc. 20th Int. Conf. Young Specialists Micro/Nanotechnol. Electron Devices (EDM)*, 2019, pp. 23–27.

[12] G. Qin et al., "Cryogenic operation of a 24 GHz MMIC SiGe HBT medium power amplifier," *Semicond. Sci. Technol.*, vol. 25, no. 12, 2010, Art. no. 125002.

[13] Y. Peng, J. Benserhir, M. Castaneda, A. Fognini, C. Bruschini, and E. Charbon, "A $0.32\times0.12\,\text{mm}^2$ cryogenic BiCMOS 0.1–8.8 GHz low noise amplifier achieving 4 K noise temperature for SNWD readout," *IEEE Trans. Microw. Theory Techn.*, vol. 72, no. 4, pp. 2179–2192, Apr. 2024.

[14] H. Rücker, J. Korn, and J. Schmidt, "Operation of SiGe HBTs at cryogenic temperatures," in *Proc. IEEE Bipolar/BiCMOS Circuits Technol. Meeting (BCTM)*, 2017, pp. 17–20.

[15] J. D. Cressler, "Silicon-germanium heterojunction bipolar transistor," in *Device and Circuit Cryogenic Operation for Low Temperature Electronics*. Boston, MA, USA: Springer, 2003, pp. 69–84.

[16] C. Enz and H.-C. Han, "Design of Cryo-CMOS analog circuits using the G_m/I_D approach," in *Proc. IEEE Int. Symp. Circuits Syst. (ISCAS)*, 2023, pp. 1–5.

[17] "CRX-4K cryogenic probe station Datasheet," Datasheet, Lake Shore Cryogenics, Westerville, OH, USA, 2023. [Online]. Available: https://www.lakeshore.com/products/categories/overview/material-characterization-products/cryogenic-probe-stations/model-CRX-4K-cryogenic-probe-station

[18] U. Stumper and T. Schrader, "Influence of different configurations of nonideal calibration standards on vector network analyzer performance," *IEEE Trans. Instrum. Meas.*, vol. 61, pp. 2034–2041, 2012.

[19] D. A. Teeter, J. R. East, R. K. Mains, and G. I. Haddad, "Large-signal numerical and analytical HBT models," *IEEE Trans. Electron Devices*, vol. 40, no. 5, pp. 837–845, May 1993.

[20] D. R. Pehlke and D. Pavlidis, "Evaluation of the factors determining HBT high-frequency performance by direct analysis of S-parameter data," *IEEE Trans. Microw. Theory Techn.*, vol. 40, no. 12, pp. 2367–2373, Dec. 1992.

[21] K. Beyzavi, K. Lee, D. Kim, M. Nathan, K. Wrenner, and S. Wright, "Temperature dependence of minority-carrier mobility and recombination time in p-type GaAs," *Appl. Phys. Lett.*, vol. 58, no. 12, pp. 1268–1270, 1991.

[22] T. Taris, A. H. M. Shirazi, and S. Mirabbasi, "Design of low power CMOS RF building blocks," in *Proc. Asia–Pacific Microw. Conf. (APMC)*, vol. 1, 2015, pp. 1–3.

[23] J. Olvera-Cervantes, J. Cressler, J. Medina-Monroy, T. Thrivikraman, B. Banerjee, and J. Laskar, "A new analytical method for robust extraction of the small-signal equivalent circuit for SiGe HBTs operating at cryogenic temperatures," *IEEE Trans. Microw. Theory Techn.*, vol. 56, no. 3, pp. 568–574, Mar. 2008.

[24] X. Jin, M. Müller, P. Sakalas, A. Mukherjee, Y. Zhang, and M. Schröter, "Advanced SiGe: C HBTs at cryogenic temperatures and their compact modeling with temperature scaling," *IEEE J. Explor. Solid-State Computat. Devices Circuits*, vol. 7, no. 2, pp. 175–183, Dec. 2021.

[25] X. Jia and G. Niu, "Impact of correlated RF noise on SiGe HBT noise parameters and LNA design implications," *IEEE Trans. Electron Devices*, vol. 61, no. 7, pp. 2324–2331, Jul. 2014.

[26] M. Rudolph, R. Doerner, L. Klapproth, and P. Heymann, "An HBT noise model valid up to transit frequency," *IEEE Electron Device Lett.*, vol. 20, no. 1, pp. 24–26, Jan. 1999.

[27] M. Seif et al., "Low frequency noise measurements of advanced BiCMOS SiGe:C Heterojunction bipolar transistors used for mm-Wave to terahertz applications," in *Proc. 22nd Int. Conf. Noise Fluctuations (ICNF)*, 2013, pp. 1–4.

[28] F. Pascal, J. Raoult, B. Sagnes, A. Hoffmann, S. Haendler, and G. Morin, "Improvement of 1/f noise in advanced 0.13 μm BiCMOS SiGe:C Heterojunction bipolar transistors," in *Proc. 21st Int. Conf. Noise Fluctuations*, 2011, pp. 279–282.

[29] C. Raya, B. Ardouin, and Z. Huszka, "Improving parasitic emitter resistance determination methods for advanced SiGe:C HBT transistors," in *Proc. IEEE Bipolar/BiCMOS Circuits Technol. Meeting*, 2011, pp. 191–194.

[30] S.-C. Huang, C.-T. Chang, C.-T. Pan, and Y.-M. Hsin, "Improved SiGe power HBT characteristics by emitter layout," *Solid-state Electron.*, vol. 52, pp. 946–951, Jun. 2008.

[31] S. J. Proctor and L. W. Linholm, "A direct measurement of interfacial contact resistance," *IEEE Electron Device Lett.*, vol. 3, no. 10, pp. 294–296, Oct. 1982.

[32] J. Krause and M. Schröter, "Methods for determining the emitter resistance in SiGe HBTs: A review and an evaluation across technology generations," *IEEE Trans. Electron Devices*, vol. 62, no. 5, pp. 1363–1374, May 2015.

[33] W. Kloosterman, J. Paasschens, and D. Klaassen, "Improved extraction of base and emitter resistance from small signal high frequency admittance measurements," in *Proc. Bipolar/BiCMOS Circuits Technol. Meeting*, 1999, pp. 93–96.

[34] L. Laurent, "Measurement of the noise temperature of an amplifier," in *Parametric Amplifiers. Philips Technical Library*. London, U.K.: Palgrave, 1973, pp. 276–296.

[35] H. A. Haus and R. B. Adler, *Circuit Theory of Linear Noisy Networks*. Cambridge, MA, USA: MIT Press, 1959.

[36] G. Niu, J. D. Cressler, S. Zhang, A. Joseph, and D. Harame, "Noise-gain tradeoff in RF SiGe HBTs," *Solid-State Electron.*, vol. 46, no. 9, pp. 1445–1451, 2002.

[37] G. Niu, "Noise in SiGe HBT RF technology: Physics, modeling, and circuit implications," *Proc. IEEE*, vol. 93, no. 9, pp. 1583–1597, Sep. 2005.

[38] Y. Peng, A. Ruffino, J. Benserhir, and E. Charbon, "A cryogenic SiGe BiCMOS hybrid class B/C mode-switching VCO achieving 201dBc/Hz figure-of-merit and 4.2 GHz frequency tuning range," in *Proc. IEEE Int. Solid-State Circuits Conf. (ISSCC)*, vol. 65, 2022, pp. 364–366.

[39] Y. Peng, J. Benserhir, Y. Zou, and E. Charbon, "A cryogenic double-IF SSB controller with image suppression and on-chip filtering implemented in 130nm SiGe BiCMOS technology for superconducting qubit control," in *Proc. Custom Integr. Circuits Conf. (CICC)*, Apr. 2024, pp. 1–2.

[40] J. Vildeuil, M. Valenza, and D. Rigaud, "CMOS 1/f noise modelling and extraction of BSIM3 parameters using a new extraction procedure," in *Proc. Int. Conf. Microelectron. Test Struct.*, 1999, pp. 206–211.
[41] "Low noise current preamplifier Datasheet," Datasheet SR570, SRS, Sunnyvale, CA, USA, 2023. [Online]. Available: https://www.thinksrs.com/products/SR570.html
[42] "N9030A PXA signal analyzer, 3 Hz to 50 GHz Datasheet," Datasheet, Keysight, Santa Rosa, CA, USA, 2023. [Online]. Available: https://www.keysight.com/us/en/product/N9030A/pxa-signal-analyzer-3Hz-50GHz.html
[43] K. Ohmori, R. Hasunuma, W. Feng, and K. Yamada, "Continuous characterization of MOSFET from low-frequency noise to thermal noise using a novel measurement system up to 100 MHz," in *Proc. Symp. VLSI Technol. (VLSIT)*, 2012, pp. 143–144.
[44] A. Bevilacqua and P. Andreani, "An analysis of $1/f$ noise to phase noise conversion in CMOS harmonic oscillators," *IEEE Trans. Circuits Syst. I, Reg. Papers*, vol. 59, no. 5, pp. 938–945, May 2012.
[45] D. Xie and L. Forbes, "Phase noise on a 2-GHz CMOS LC oscillator," *IEEE Trans. Comput. Aided Design Integr. Circuits Syst.*, vol. 19, no. 7, pp. 773–778, Jul. 2000.
[46] S. L. J. Gierkink, E. A. M. Klumperink, A. P. van der Wel, G. Hoogzaad, E. A. J. M. van Tuijl, and B. Nauta, "Intrinsic 1/f device noise reduction and its effect on phase noise in CMOS ring oscillators," *IEEE J. Solid State Circuits*, vol. 34, no. 7, pp. 1022–1025, Jul. 1999.
[47] S. Gierkink, A. P. V. D. Wel, G. Hoogzaad, E. Klumperink, and A. V. Tuijl, "Reduction of the 1/f noise induced phase noise in a CMOS ring oscillator by increasing the amplitude of oscillation," in *Proc. IEEE Int. Symp. Circuits Syst.*, vol. 1, 1998, pp. 185–188.
[48] T. Yoshida, N. Ishida, M. Sasaki, and A. Iwata, "Low-voltage, low-phase-noise ring voltage-controlled oscillator using 1/f-noise reduction techniques," *Jpn. J. Appl. Phys.*, vol. 46, no. 4S, p. 2257, 2007.
[49] G. Ghibaudo, O. Roux, C. Nguyen-Duc, F. Balestra, and J. Brini, "Improved analysis of low frequency noise in field-effect MOS transistors," *Physica Status Solidi (a)*, vol. 124, no. 2, pp. 571–581, 1991.
[50] R. Jindal and A. Van Der Ziel, "Model for mobility fluctuation 1/f noise," *Appl. Phys. Lett.*, vol. 38, no. 4, pp. 290–291, 1981.
[51] A. McWhorter, "1/f noise and germanium surface properties," in *Semiconductor Surface Physics*, R. H. Kingston, Ed., Philadelphia, PA, USA: Univ. Pennsylvania, 1957, pp. 207–228.